2D TMD MATERIALS: ATOMIC STRUCTURES AND ELECTRONIC PROPERTIES

LIM RONG SHENG

SUPERVISOR

PROFESSOR ANDREW WEE THYE SHEN

CO-SUPERVISOR

DR HUANG YULI

A THESIS SUBMITTED

FOR PARTIAL FULFILMENT FOR THE DEGREE OF BACHELOR OF SCIENCE

WITH HONOURS IN PHYSICS

DEPARTMENT OF PHYSICS

NATIONAL UNIVERSITY OF SINGAPORE

2014

Acknowledgement

First and foremost, I would like to express my deepest gratitude towards my supervisors, Prof. Andrew Wee and Dr Huang Yuli. Their patient guidance and advice has proved invaluable; without which it would not be possible for me to acquire the necessary skills to bring this project to fruition. In spite of having a full workload, their meticulous and tireless review of my manuscripts and experimental work, as well as expressing such care and concern for their students has made an impression on me regarding the immense dedication and professionalism they take toward their craft.

In particular, I would like to give my special thanks to Dr Huang Yuli for her constructive suggestions and support by means of spending much time and effort in addressing any queries of mine. She selflessly taught me many experimental techniques, data analysis and operational skills, while providing me valuable insights to the life of a researcher.

I would like thank Dr Li Hai from Nanyang Technological University, Prof Li Lain-jong from Academia Sinica Taiwan and Prof Eda Goki from the National University of Singapore for kindly providing samples for study.

I am also thankful for my fellow students and friends, both from within and without the Surface Science Laboratory and the Physics Department. Their kind camaraderie and support provided is priceless and will be highly cherished.

Last but not least, I am also grateful for the love and support that my family has shown me over this period. Their support has constantly spurred me to greater heights.

Table of Contents

Summary

In this thesis, we investigated the surface structural and electronic properties of single- to few-layered MoS_2 on HOPG substrates obtained via three different preparation methods. Scanning tunneling microscopy and spectroscopy measurements are used to visualize the physical and electronic structures at the surface. *In situ* growth of MoS_2 on Ag(111) surfaces were also attempted.

In the first method, the few-layered MoS_2 was mechanically exfoliated and deposited onto a HOPG substrate. This yielded regions of about 20 μm of few-layered MoS_2. This MoS_2 sample was found to be with a relatively defect-rich, present on about 10% of the surface area, with sizes of the defects ranging from 2 nm to 10 nm. Extensive defects manifested as ripples and nanoclusters, modifying the topographical images obtained by STM. Possible causes of these defects were thought to be the presence of vacancies, impurities, or excess stress.

In the second method, MoS_2 was grown directly onto HOPG using the CVD method. This sample consisted of MoS_2 monolayers of about hundreds of nanometers in size. On about 1% of the sample surface, there were observable defects. These defects appear as different features under different scanning biases, and are attributed to single sulfur vacancies. The bandgap of the monolayers was also determined using STS to be about 2.4 eV.

In the third method, MoS_2 was grown using CVD which is then chemically transferred onto HOPG. This sample contains ~50 μm MoS_2 monolayers and its bandgap was determined at about 2.25 eV.

In both CVD grown samples, direct-grown or transferred, monolayer MoS_2 were observed to have defects of the same nature, present on about 1% of the surface area. In addition, moiré

patterns corresponding to the lattice mismatch of MoS_2 and the underlying HOPG substrate of about 1.2 nm were also observed.

In light of the defects present in the above mentioned MoS_2 samples created through mechanical exfoliation and CVD, a fourth method, *in situ* ultrahigh vacuum growth, was attempted in hopes of improving the quality of production, with more consistent and larger area of monolayer growth with fewer defects. Using this method, we were able to consistently obtain $(MoO_3)_x$ intermediates on Ag(111) substrates, with recurring 4-lobed and 3-lobed nanoparticles and regular hexagonal nanoarrays. However, we were unable to obtain MoS_2 after evaporating sulfur onto the intermediary oxide film so far. More intensive efforts will be devoted to this *in situ* growth.

List of Figures

List of Tables

List of Abbreviations

2D	Two-Dimensional
Ag	Silver
Ar	Argon
Au	Gold
ARPES	Angel-resolved Photoemission Spectroscopy
CVD	Chemical Vapour Deposition
DOS	Density of States
E_f	Fermi Level
HOPG	Highly Ordered/Oriented Pyrolytic Graphite
LDOS	Local Density of States
Mo	Molybdenum
MoO_3	Molybdenum trioxide
MoS_2	Molybdenum Disulfide
$MoSe_2$	Molybdenum Diselenide
PMMA	Poly(methyl methacrylate)
S	Sulfur
Si	Silicon
SiO_2	Silicon Dioxide
STM	Scanning Tunnelling Microscopy
STS	Scanning Tunnelling Spectroscopy
TMD	Transition Metal Dichalcogenide
UHV	Ultra High Vacuum

Chapter 1: Introduction

1.1 Properties of Transition Metal Dichalcogenides

Since the discovery of graphene in 2004[1-4], much research has been extensively performed as a potential material for the next generation of electronic devices. This extraordinary two-dimensional (2D) allotrope of carbon is both chemically inert and highly stable, making it an ideal alternative to bulk graphite[3, 5-6]. However, the lack of a band gap[5] presents challenging problems in semiconductor devices. Its inert nature can be activated by functionalization with foreign molecules[7], however, this causes the loss of some of its properties.

Progress in graphene research had a spillover effect by way of leading to an interest in other 2D materials. Of particular interest has been research in transition metal dichalcogenides (TMDs), which have a similar lamellar structure of graphene. TMDs, as its name suggests, is made up of a transition metal in the group 4-10 of the periodic table and a chalcogen, with a general formula of MX_2, M being the transitional metal and X being the chalcogen. Apart from being naturally abundant[8, 9], TMDs also have a bandgap akin to that of semiconductors. The versatility observed in TMDs in terms of the diverse range of properties depending on its composition poses exciting new possibilities in a wide array of applications.

Crystalline TMDs forms a layered structure not unlike graphite, leading to strong directional dependency in their electrical, chemical, mechanical and thermal properties[10]. Each layered structure is typically 6-7 Å thick, consisting of a hexagonal packed layer of transition metal atoms sandwiched between two layers of chalcogen atoms (Figure 1.1a). These intra-layer metal atoms are bonded covalently to the chalcogen atoms while the layers are weakly

bonded by van der Waals forces. Each MX_2 monolayer exists in either of 2 phases; trigonal prismatic or trigonal antiprismatic coordination[11] shown in Figure 1.1b and 1.1c.

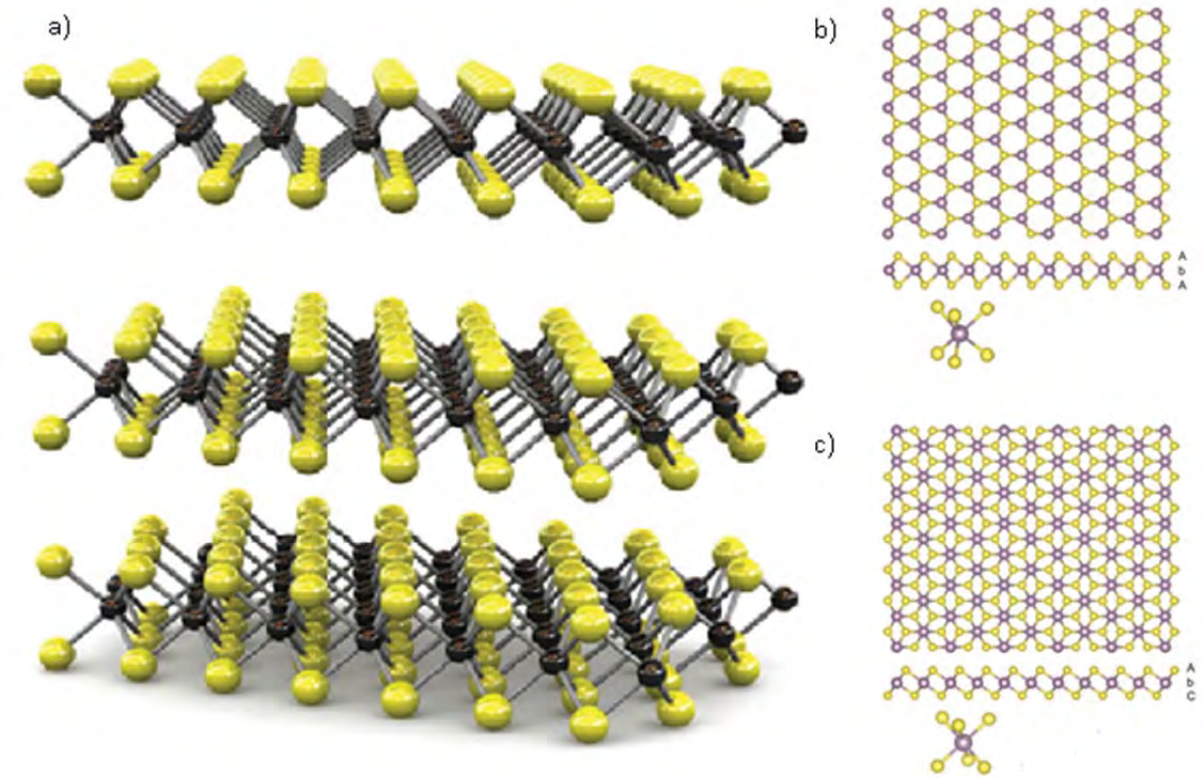

Figure 1.1 (a-c) Ball and stick models representing the TMDs. Chalcogens are represented by the yellow balls while the transition metals are represented by the black and purple balls in (a), and (b) and (c) respectively. (a) The bonds within the layer are covalent, while the inter-layer bonds are bonded via weak van der Waals forces. (b) shows the trigonal prismatic (D_{3h}) coordination while (c) shows the trigonal antiprismatic (O_h) coordination. (a) Adapted from reference 13; (b-c) Adapted from reference 11.

The electronic properties of TMDs depend strongly on the coordination of the transition metal atom. Different coordination of the transition metal atom affect the degeneration of the non-bonding d orbitals. The progressive filling of these orbitals across different groups account for the diverse electronic properties of TMDs: exhibiting metallic characteristic with partially filled orbitals while being semiconductive with fully filled orbitals. The chalcogen also has a noticeable effect on the bandgap: as the chalcogen increases in atomic number, the d bands broaden, causing a gradual decrease in the bandgap[12].

1.2 Thesis Objectives

In the light of the remarkable properties and potential practical applications that TMDs hold, it is of great interest to further investigate its full potential. In being able to better understand TMD's growth methods and mechanisms, as well as its structural and electronic properties, the door to industrial production and applications can be unlocked.

The MoS_2 samples examined in this thesis will be studied via two experimental methods: scanning tunneling microscopy (STM) measurements to provide atomic-scale imaging, and scanning tunneling spectroscopy (STS) to probe the electronic structure. Samples prepared by different methods will be investigated and compared. The first sample is an MoS_2 sample that has been mechanically exfoliated and deposited onto a HOPG substrate obtained from Dr Li Hai, Nanyang Technological University of Singapore. The second MoS_2 sample is obtained from Prof Li Lain-jong's group from Academia Sinica Taiwan, which was grown directly onto HOPG using the chemical vapour deposition (CVD) method. The third sample is an MoS_2 sample grown using CVD, which was subsequently transferred onto a HOPG substrate by Prof Eda Goki's group from the National University of Singapore. Finally, *in situ* growth of MoS_2 in ultrahigh vacuum will be attempted.

In this thesis, the working principles of the relevant techniques used for STM measurements will be discussed first, followed by an in-depth presentation of STM data to discuss the atomic structure as well as the electronic properties of few-layered MoS_2.

References

1 Novoselov, K. S.; Geim, A. K.; Morozov, S. V.; Jiang, D.; Katsnelson, M. I.; Grigorieva, I. V.; Dubonos, S. V.; and Firsov, A. A.; *Nature* **438**, 197-200 (2005).

2 Novoselov, K. S.; Jiang, D.; Schedin, F.; Booth, T. J.; Khotkevich, V. V.; Morozov, S. V.; and Geim, A. K.; *Proc. Natl. Acad. Sci. USA* **102**, 10451-10453 (2005).

3 Novoselov, K. S.; Geim, A. K.; Morozov, S. V., Jiang, D.; Zhang, Y.; Dubonos, S. V.; Grigorieva, I. V.; and Firsov, A. A.; *Science* **306**, 666-669 (2004).

4 Zhang, Y.; Tan, Y.; Stormer, H. L.; and Kim, P.; *Nature* **438**, 201 (2005).

5 Castro Neto, A. H.; Guinea, F.; Peres, N. M. R.; Novoselov, K. S.; and Geim, A. K.; *Rev. Mod. Phys.* **81**, 109–162 (2009).

6 Geim, A. K.; *Science* **324**, 1530–1534 (2009).

7 Loh, K. P.; Bao, Q. L.; Eda, G.; and Chhowalla, M.; *Nature Chem.* **2**, 1015–1024 (2010).

8 Mak, K. F.; Lee, C.; Hone, J.; Shan, J.; and Heinz, T. F.; *Phys. Rev. Lett.* **105**, 136805 (2010).

9 Splendiani; A.; Sun, L.; Zhang, Y.; Li, T.; Kim, J.; Chim, C.; Galli, G.; and Wang, F.; *Nano Lett.* **10**, 1271–1275 (2010).

10 Wilson, J. A.; Di Salvo, F. J.; and Mahajan, S.; *Adv. Phys.* **24**, 117–201 (1975).

11 Chhowalla, M.; Shin, H. S.; Eda, G.; Li, L.; Loh, K. P.; and Zhang, H.; *Nature Chemistry* **5**, 263–275 (2013).

12 Wilson, J. A.; and Yoffe, A. D.; *Adv. Phys.* **18**; 193–335 (1969).

13 Radisavljevic, B.; Radenovic, A.; Brivio, J.; Giacometti, V.; and Kis, A; *Nat. Nanotechnology* **6**, 147−150 (2011).

Chapter 2: Experimental Method

2.1 Scanning Tunneling Microscopy/Spectroscopy

The invention of the STM by Gerd Binning and Heinrich Rohrer of IBM Zürich in 1981 confers the ability to image a surface with atomic resolution, allowing for exciting possibilities to delve into the nanoscale, and also earning its inventors the Nobel Prize in Physics just five years later in 1986[1-5]. STM is able to probe the local atomic-scaled physical and electronic details of a surface with high clarity that is incomparable to other techniques. This unique ability of the STM makes it ideal as a tool to characterize 2D materials.

2.1.1 Operating Principles: Scanning Tunneling Microscopy

The primary phenomenon exploited by STM is the quantum mechanical tunneling of electrons between the surface of a sample and the scanning tip, through a potential barrier posed by the space between them. This tunneling occurs when a potential difference is applied across the sample and the scanning tip. When the gap between the sample surface and the scanning tip is small, the probability of electron tunneling can be calculated from the Fermi golden rule. By approximating the potential barrier between the surface and the tip as a series of square potential well using the Wentzel-Kramers-Brillouin approximation[6], we obtain the tunneling probability in Equation 2.1.

$$T(E, eV, z) \propto e^{-\frac{2z\sqrt{2m}}{\hbar}\sqrt{\frac{\phi_s+\phi_t}{2}+\frac{eV}{2}-E}} \tag{2.1}$$

With E being the energy of the electronic state, m the mass of the electron, z the separation between the surface and the tip and ϕ_s and ϕ_t being the work function of the sample and the tip respectively.

The potential barrier is approximated by the average of the two work functions and it can be seen that the tunneling probability, and therefore, the tunneling current is exponentially inversely proportional to the tip-surface separation. It is this high sensitivity to the separation at close proximity which gives rise to the atomic resolution of the STM.

In addition to the tip-surface separation, the tunneling current is also affected by the available electrons for tunneling and also the available states for these electrons to tunnel into. Thus, with the applied potential difference V, and the tunneling probability T, the current can be described by Equation 2.2.

$$I = \frac{4\pi}{\hbar}\int_0^{eV}\{[f(E_f - eV + \varepsilon) - f(E_f + \varepsilon)]\rho_s(r, E_f + \varepsilon)\rho_t(r, E_f - eV + \varepsilon)\}Td\varepsilon \qquad (2.2)$$

With ρ_s and ρ_t being the density of states of the surface and tip respectively as a function of position r, and energy ε with respect to the Fermi level E_f. The function f, is the Fermi-Dirac distribution, which states the electronic occupancy at a given energy level.

When the applied bias voltage is small, where $eV << \phi$, the density of states of the tip, ρ_t can be approximated as a constant in the small range about the Fermi level. The height of the potential barrier can also be approximated to be independent of the bias applied. When experiments are carried out at low temperatures of 77 K, the Fermi-Dirac distribution is also approximated as a step function. With these approximations, the tunneling current simplifies to Equation 2.3.

$$I = \frac{4\pi}{\hbar}\rho_t(0)e^{-\frac{2z\sqrt{2m\phi}}{\hbar}}\int_0^{eV}\rho_s(r, E)dE \qquad (2.3)$$

Thus, it can be seen that the tunneling current is dependent on both the tip-surface separation and the density of states of both tip and the surface[7]. This is illustrated in Figure 2.1.

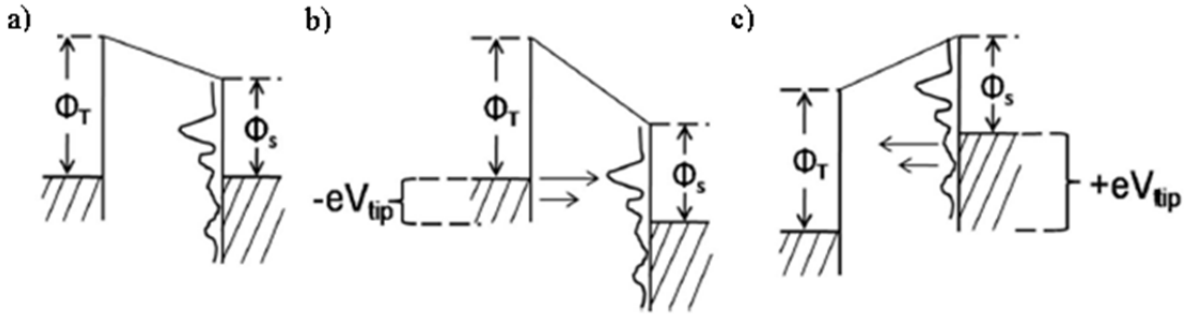

Figure 2.1 (a-c) Energy level diagrams for the sample and the tip, with ϕ_s and ϕ_t being the work function, dashed lines being the vacuum level, solid horizontal lines being the Fermi level and the curve being the sample density of states. (a) Sample and tip at thermal equilibrium with no applied bias. Fermi level aligned and no tunneling occurs. (b) Negative tip bias is applied, causing the Fermi level of tip to move higher than that of the sample. Electrons thus tunnel from the occupied tip states into the unoccupied states of the sample. (c) Positive tip bias is applied, causing the Fermi level of tip to move lower than that of the sample. Electrons thus tunnel from the occupied sample states into the unoccupied states of the tip. Adapted from reference 13.

As the tip is raster scanned across the surface, the tip-surface separation and the local electronic density of states will differ, causing changes to the tunneling current. This tunneling current is then amplified and sent to the controller for interpretation, translating the variations in current into spatial variation in surface topography, and/or the variation in the electronic structures of the individual atom being probed. The tip is mounted on a piezoelectric material which is highly sensitive to the voltage applied to it, thus allowing atomic precision in controlling its vertical and lateral positions.

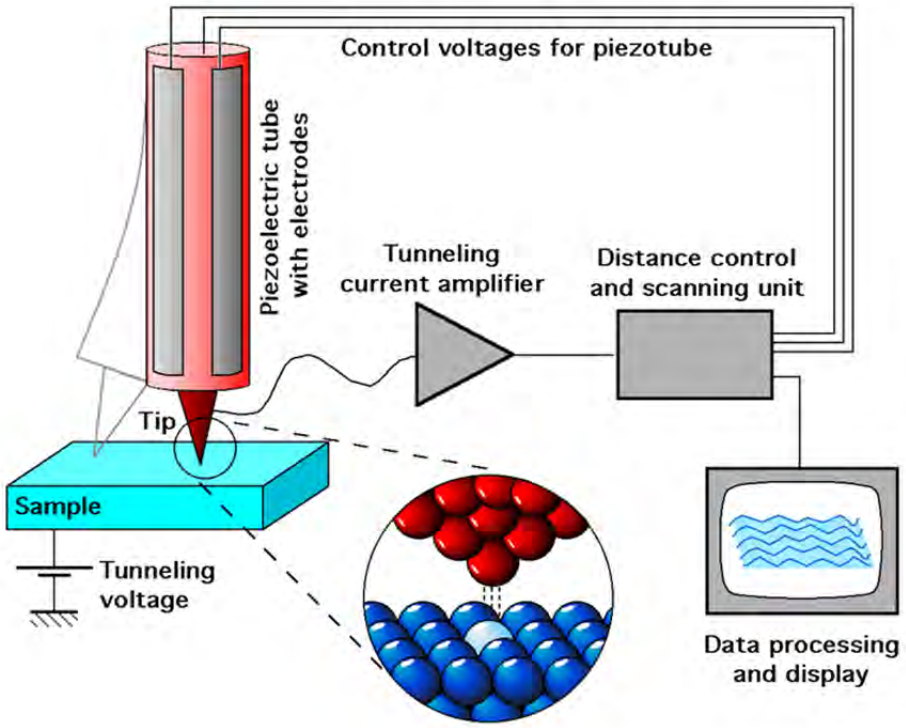

Figure 2.2 Schematic of an STM set up. Obtained from Michael Schmid, Wikipedia.

The STM is able to scan in two modes. The first of which is the constant current mode, whereby the tunneling current is kept constant during the scan via a feedback loop. As the current increases or decreases during the scan due to changes in tip separation and/or electronic density, the feedback loop will cause the tip to retract from or approach the surface so as to keep the tunneling current constant. This variation in tip height is then recorded as an STM topographical image. The second scanning mode possible is the constant height mode, where the tip height is maintained constant as the tip scans across the surface. Here, the variations in the tunneling current are registered as the STM image. In the experiments describe in this thesis, the constant current mode is always used, to obtain maximal resolution and to prevent the tip from crashing into the surface.

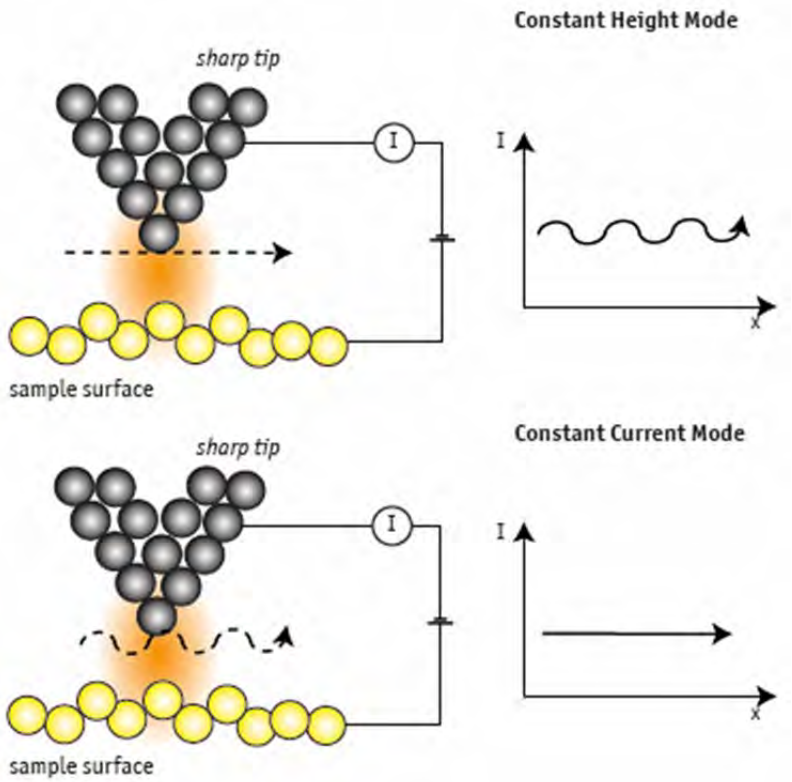

Figure 2.3 Schematic of the two scanning modes, constant height mode (top), and constant current mode (bottom). Obtained from attocube systems AG.

2.1.2 Operating Principles: Scanning Tunneling Spectroscopy

As mentioned in the previous section, since tunneling is affected by the sample density of states, the STM probe can also be used in a technique called STS to measure the local density of states at a particular energy level. This can be achieved simply by measuring the differential tunneling current, dI/dV. By taking the derivative of equation 2.3, we obtain the following relation:

$$\frac{dI}{dV} \propto \rho_s(r, eV) \tag{2.4}$$

It is immediately pronounced that the differential tunneling conductance is directly proportional to the density of states of the sample at the given energy.

During STS measurement, the feedback loop is turned off to keep the tip-sample separation constant, removing the height dependence of the tunneling current. Thereafter, the applied bias is then varied and the resultant variation in the tunneling current is measured, during which the differential tunneling current is obtained. Usually, the tunneling current is perturbed by a wide-band current noise from mechanical vibrations and from thermal noise generated in the current voltage convertor. In order to obtain a high signal to noise ratio, the applied bias is modulated with a small sinusoidal alternating voltage and thus causing the same modulation in the tunneling current. The frequency of the modulation voltage is set to a much higher frequency than the regulating speed of the feedback loop to prevent any interference to it. The amplified modulated current will then be multiplied with the reference modulating signal and phase shifted by φ by a Lock-In amplifier giving an output as follows:

$$\underbrace{\sin(\omega_m t+\varphi)}_{reference}\times\left(\underbrace{\rho_s(\epsilon)eV_m\sin(\omega_m t+\varphi_0)}_{signal}+\underbrace{\int_0^\infty a_\omega\sin(\omega t+\varphi_\omega)d\omega}_{noise}\right) \tag{2.5}$$

$$=\frac{1}{2}\rho_s(\epsilon)eV_m[\cos(\varphi-\varphi_0)+\cos(2\omega_m t+\varphi+\varphi_0)]+\cdots$$

where φ is the phase shift by the Lock-In amplifier, ρ_s is the local density of state, ω_m, and V_m is the modulation frequency and voltage respectively and a_ω and φ_ω being the amplitude and phase of the noise. All overlaying noise with phases uncorrelated with the reference is filtered out by a frequency low-pass filter, whereas the contribution of the input signal, having the same frequency of the reference and the phase angle φ-φ_0 is converted to a direct current signal. This converted signal is directly proportional to the modulation amplitude and local density of states of the surface. This allows us to strongly suppress shot noise thus enhancing the signal quality[8].

With the capabilities of real-space atomic resolution imaging, the STM offers strong advantages over other tools for the investigation of surface phenomena, and the characterization of the topographical and electronic properties at nanoscale.

2.2 Experimental System

Indeed, STM studies of MoS_2 had been carried out[9-11] but previous studies were limited, with focus mainly on probing multilayer MoS_2, and nanoclusters with sizes of tens of nanometers on Au(111).

In our experiments, low temperature STM (LT-STM), were carried out in a custom-build multi-chamber ultrahigh vacuum (UHV) system with a base pressure of less than 10^{-10} mbar. This system houses an "Omicron" LT-STM interfaced to a "Nanonis" controller[12]. Analysis and processing of the STM images were carried out on the WSxM[13] and Gwyddion[14] software. The LT-STM is designed to operate at a two different temperatures, depending on the coolant used. Liquid helium is used to cool the sample to 4 K, whereas liquid nitrogen is used to cool it to 77 K. The low temperature minimizes thermal diffusion of atoms or molecules and any thermal broadening of electron energy states, thus maintaining a stable scanning interface and a better image quality. The substrate is grounded during scanning while the bias voltage is applied at the scanning tip. In this study, all samples were cooled to 77 K and STM images were recorded with tunneling current ranging from 80 pA to 110 pA.

Molecular deposition is carried out via thermal evaporation from effusion cells in the preparation chamber as required, before being transferred to the STM chamber for *in situ* scanning. For externally grown samples, they were also degassed in the preparation chamber before being transferred to the adjacent chamber for scanning. This separate chamber has a base pressure of below 5×10^{-10} mbar and all preparatory work was done in it to minimize outgassing in the STM chamber in order to maintain the UHV environment. The ultrahigh

vacuum environment of the system ensures the low level of contamination. A photograph of the experimental system used is shown in Figure 2.4.

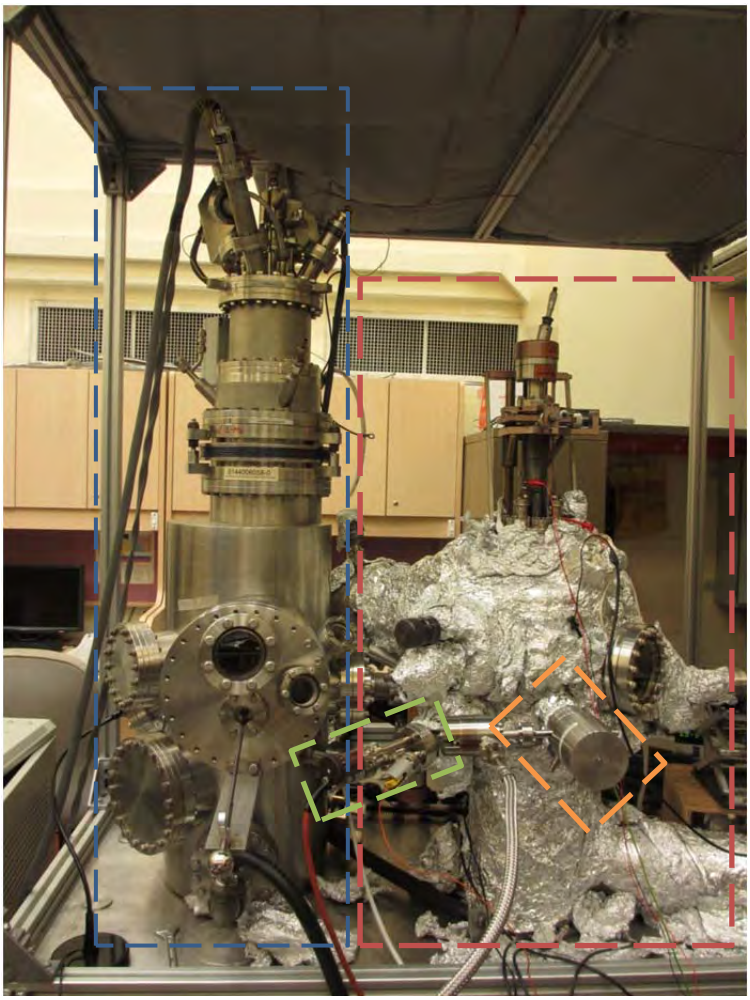

Figure 2.4 Photograph of the UHV system used in the experiments. The LT-STM chamber is outlined in blue dashed lines, the preparation chamber outlined in red dashed lines, the effusion cell outlined in green dashed lines and the sputtering gun outlined in orange.

References

1 Binnig, G.; and Rohrer, H.; *Rev. Mod. Phys.* **59**, 615-625 (1987).

2 Binnig, G.; Rohrer, H.; Gerber, C.; and Weibel, E.; *Phys. Rev. Lett.* **49**, 57-61 (1982).

3 Wiesendanger, R.; *Scanning Tunneling Microscopy III: Theory of STM and Related Scanning Probe Methods (Springer-Verlag, 1993).*

4 Güntherodt, H. J.; and Wiesendanger, R.; *Scanning Tunneling Microscopy I: General Principles and Applications to Clean and Adsorbate-covered Surfaces (Springer-Verlag,1994).*

5 Güntherodt, H. J.; and Wiesendanger, R.; *Scanning Tunneling Microscopy II: Further Applications and Related Scanning Techniques (Springer, 1995).*

6 Lindsay, S.; *Introduction to Nanoscience* (Oxford University Press, 2010).

7 Hamers, R. J.; *Annu. Rev. Phys. Chem.* **40**, 531-559 (1989).

8 Ternes, M.; *Scanning Tunneling Spectroscopy at the Single Atom Scale;* Thèse no. 3465, École Polytechnique Fédérale De Lausanne (2006).

9 Helveg, S.; Lauritsen, J. V.; Lægsgaard, E.; Stensgaard, I.; Nørskov, J. K.; Clausen, B. S.; Topsøe, H.; and Besenbacher, F.; *Phys. Rev. Lett.* **84**, 951-954 (2000).

10 Lauritsen, J. V.; Kibsgaard, J.; Helveg, S.; Topsøe, H.; Clausen, B. S.; Lægsgaard, E.; and Besenbacher, F.; *Nat Nanotechnol* **2**, 53-58 (2007).

11 Tuxen, A.; Kibsgaard, J.; Gøbel, H.; Lægsgaard, E.; Topsøe, H.; Lauritsen, J. V.; and Besenbacher, F.; *ACS Nano* **4**,4677-4682 (2010)

12 Wong, S. L.; Huang, H; Huang, Y. L.; Wang, Y. Z.; Gao, X. Y.; Suzuki, T.; Chen, W.; and Wee, A. T. S.; *Phys. Chem. C* **114**, 9356-9361 (2010).

13 Horcas, I.; Fernández, R.; Gómez-Rodríguez, J. M.; Colchero, J. Gómez-Herrero, J.; and Baro, A. M.; *Rev. Sci. Instrum.* **78**, 013705 (2007).

14 Nečas, D; and Klapetek, P; *Cent. Eur. J. Phys.* **10(1)**, 181-188 (2012).

Chapter 3: MoS_2 Thin Films

3.1 Introduction

After the discovery of graphene as a potential silicon replacement in electronics due to their advantages of scaling, other two dimensional materials such as TMDs have also attracted much attention due to the presence of a bandgap, diverse chemistry and abundance in nature[1, 2].

MoS_2 is one such TMD which had garnered significant interest in the recent times. MoS_2 has had a long history of being used as a dry lubricant, where the readily cleaving layered structure, stability at high temperatures, and resistance to oxidation has made it ideal for this purpose[3]. However, it is only in the fairly recent years in which interest has surfaced regarding its electronic properties.

Bulk MoS_2 exhibits an indirect bandgap of 1.2 eV[4], which gradually increases to a direct bandgap[2, 5-7] of 1.8 eV[6] as the number of layers decreases to a single layer as a result of quantum confinement[7]. The lattice constant of MoS_2 is 3.131 Å at 77 K[8]. A single S-Mo-S layer is 6.5 Å thick and can be easily cleaved off bulk crystal using top-down processes such as the micromechanical cleavage technique[9, 10] used with graphene, lithium-based intercalation[11, 12], liquid phase exfoliation[13], or grown with bottom up process such as CVD using Mo and S precursors[14-17]. Theoretical calculations show that strong spin-orbit coupling causes the valance band at the energy minimas of the first Brillouin zone to split opposite to each other. This give rise to coupling between the spin and the valley degrees of freedom, and two valleys of the same energy but with different momentum values[18-21]. Incoming polarized photons interact with the spin of the holes, pushing them preferentially into one of the two valleys. This valley polarization is preserved during subsequent recombination resulting in the emission of polarized photons, which allows for the formation of valleytronic devices.

STM studies have also been performed on MoS_2 nanoparticles on Au(111)[22]. It was found that MoS_2 forms triangular nanoparticles with sulfur termination edges. These edge sulfur atoms are shifted half the lattice constant[22] and there is a propensity for them to form S_2 dimers, giving rise to higher occurrences of nanoclusters having an even number of edge sulfur atoms[23]. These sulfur atoms at the edge and corners of the nanoparticles, or rather, their vacancies, poses as active sites for the absorption of sulfur, making it useful as a catalyst for desulfurization in the petrochemical industry.

MoS_2 is the first candidate to be studied because of its semiconductor bandgap and high tensile strength, which gives it possible potential for applications in electronic devices.

3.2 Mechanically Exfoliated MoS_2

MoS_2 is made up of covalently bonded molybdenum and sulfur sandwich layers which are held together by weak van der Waals forces. One common way to obtain a 2D sample of it is via mechanical exfoliation from bulk MoS_2[2, 24-26]. The sample obtained from Dr Li Hai, NTU, was fabricated by via the scotch tape-based mechanical exfoliation method, which has been widely used in the fabrication of graphene. Few-layered MoS_2 films were deposited onto a freshly cleaned HOPG substrate for STM measurements. An optical microscopy image of the substrate as shown in Figure 3.1 shows sparsely spaced flakes of few-layered MoS_2 on the surface of about 20 μm in size highlighted by red circles. The sample was degassed at 270 ^{o}C overnight for about 12 hours.

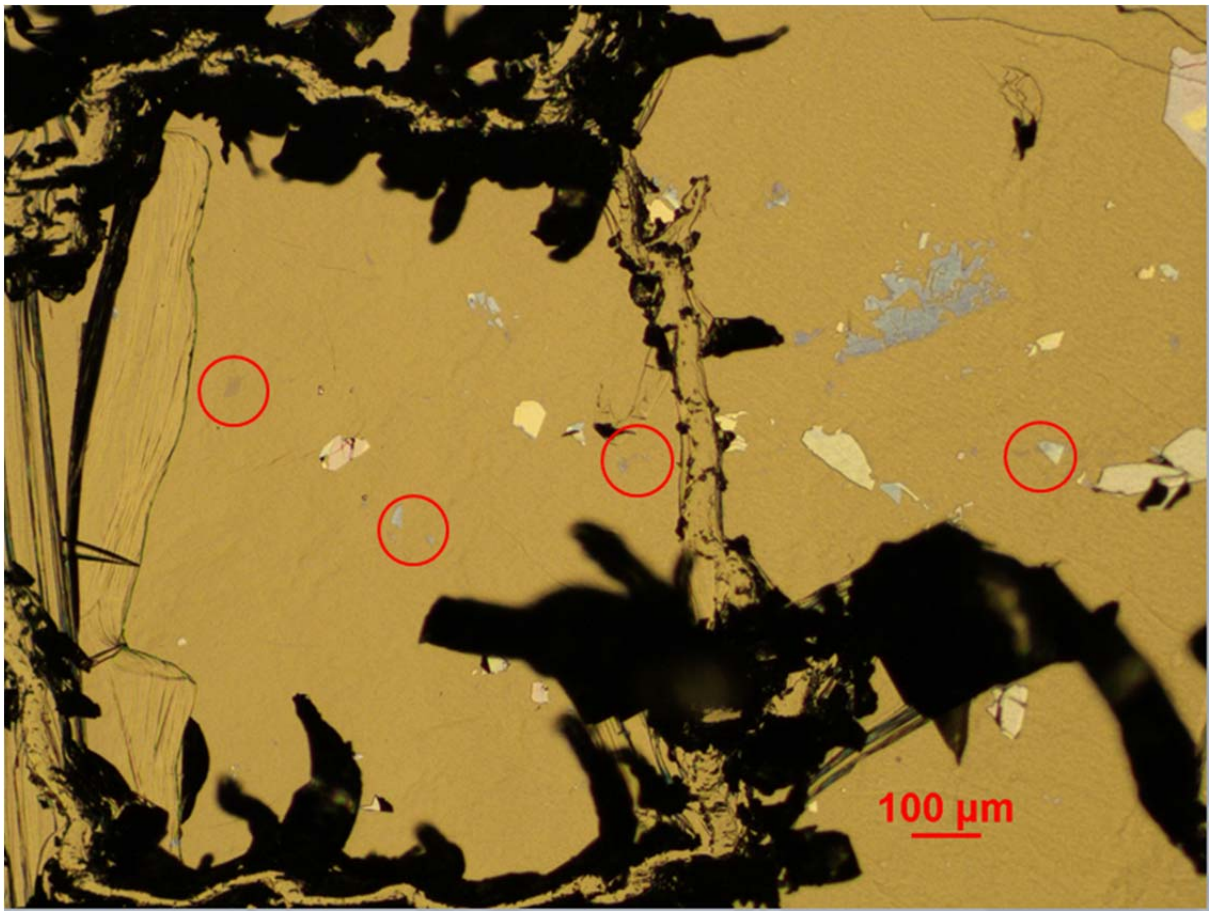

Figure 3.1 Optical microscopy image of the mechanically exfoliated MoS_2. The red circles show the locations of the MoS_2 thin films.

The grains of few-layered MoS_2 on HOPG were confirmed via STM imaging as shown in Figure 3.2. The number of layers present was determined by the height profile across the distinct boundaries, and the terrace marked by the pink line was determined to be four layers. As STM is chemically indifferent, the regions of HOPG and MoS_2 were distinguished based on their differences in crystallographic period (Figure 3.3a). The HOPG was found to have a triangle lattice, with period of 2.5±0.1 Å, corresponding to 2.46 Å as stated in the literature[27]. On the other hand, the MoS_2 regions were found to have a triangle lattice with a period of 3.2±0.1 Å, corresponding to literature values of 3.13 Å[8].

STS was also performed on the two regions (Figure 3.3b) with a lock-in voltage and frequency of 40 mV and 625 Hz respectively. For HOPG, there was no distinct flat region

observed in the spectrum obtained, indicating there is no bandgap, whereas MoS_2 had a bandgap of about 1.45 eV, which is close to the bulk 1.2 eV. It is noted that the bandgap is asymmetric about the Fermi level, where the conduction band minimum pinning at about 0.3 eV below E_f.

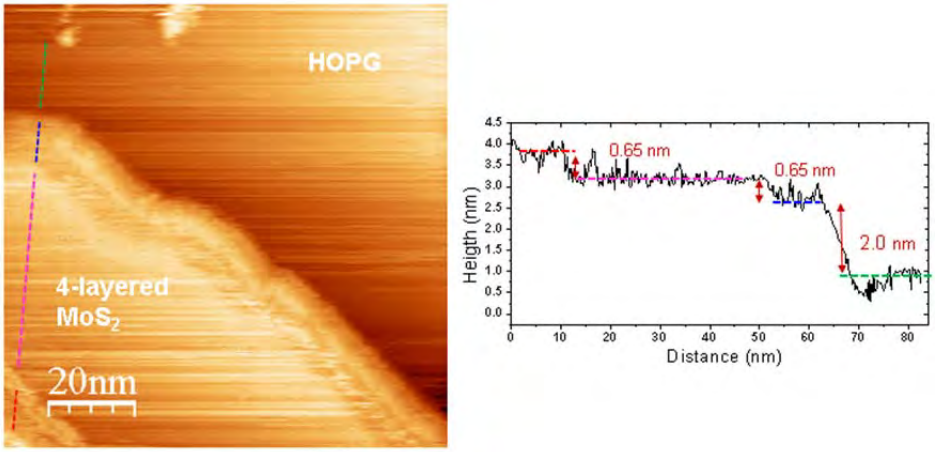

Figure 3.2 100 nm × 100 nm STM image taken of the mechanically exfoliated MoS_2 on HOPG at tip bias of 1.5 V (left), with the corresponding height profile of the dashed line(right).

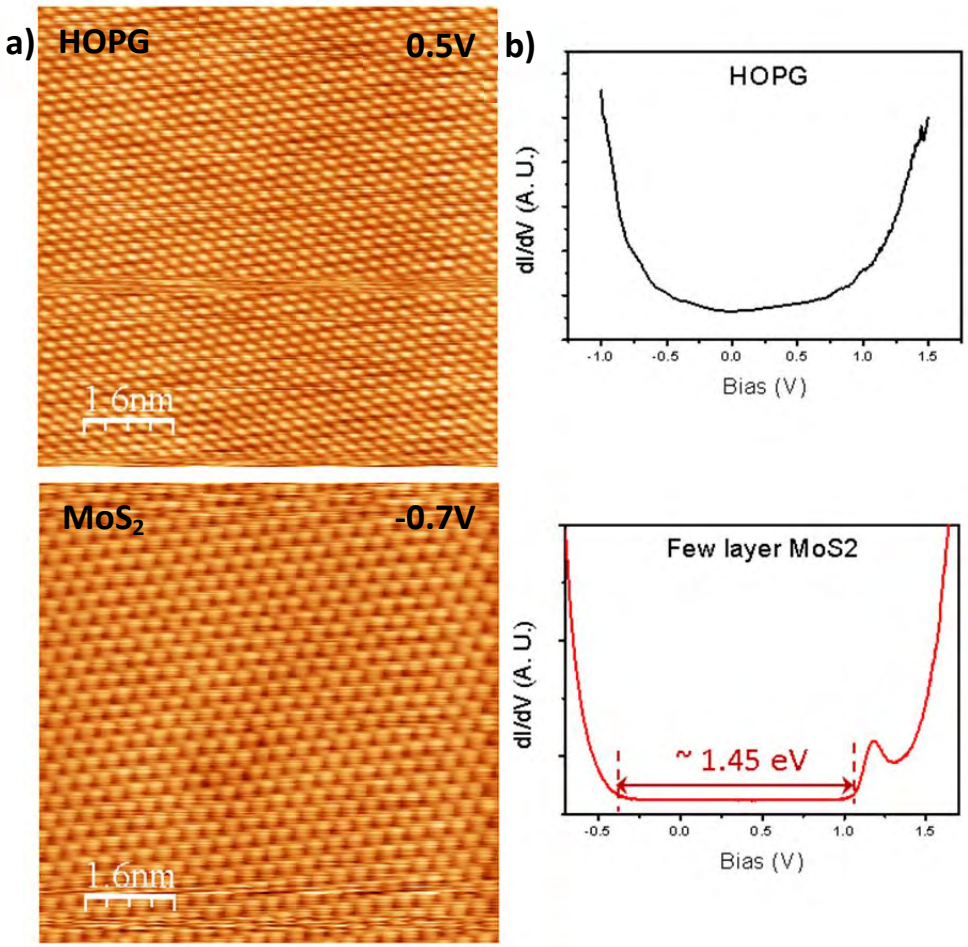

Figure 3.3 (a) 8 nm × 8 nm STM images of HOPG taken at a tip bias of 0.5 V (top), and of MoS_2 taken at a tip bias of -0.7 V (bottom). (b) STS of HOPG (top) and MoS_2(bottom).

Large-scale STM imaging of the sample reveals that the mechanically exfoliated MoS_2 has many defects, as shown in Figure 3.4. In principle, there are two types of defects which manifested themselves as ripples and nanoclusters, as shown in high resolution images of Figure 3.5a-c and Figure 3.5d respectively. The ripple-type defects modified the MoS_2 topographical images slightly. There are many possible origins of these defects, including presence of vacancies, impurities, or excess stress like those present in graphene[26, 28]. However, based on current STM experimental data, it is not possible to determine which the most likely cause is. More detailed studies and theoretical calculations will be performed in the near future to probe and further understand these defects.

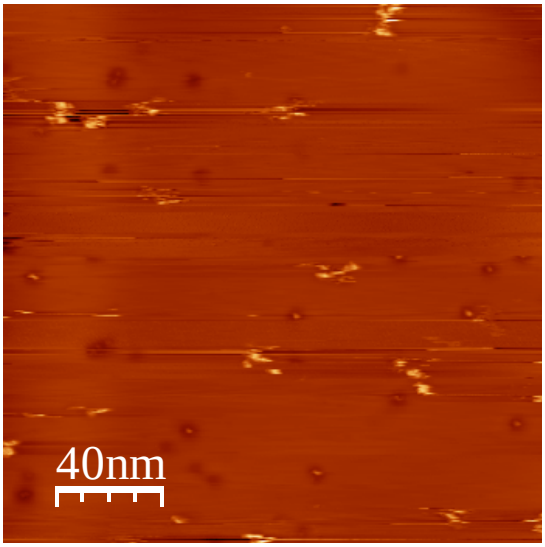

Figure 3.4 200 nm × 200 nm STM image of the MoS_2 film showing a variety of defects taken at a tip bias of 1.6 V.

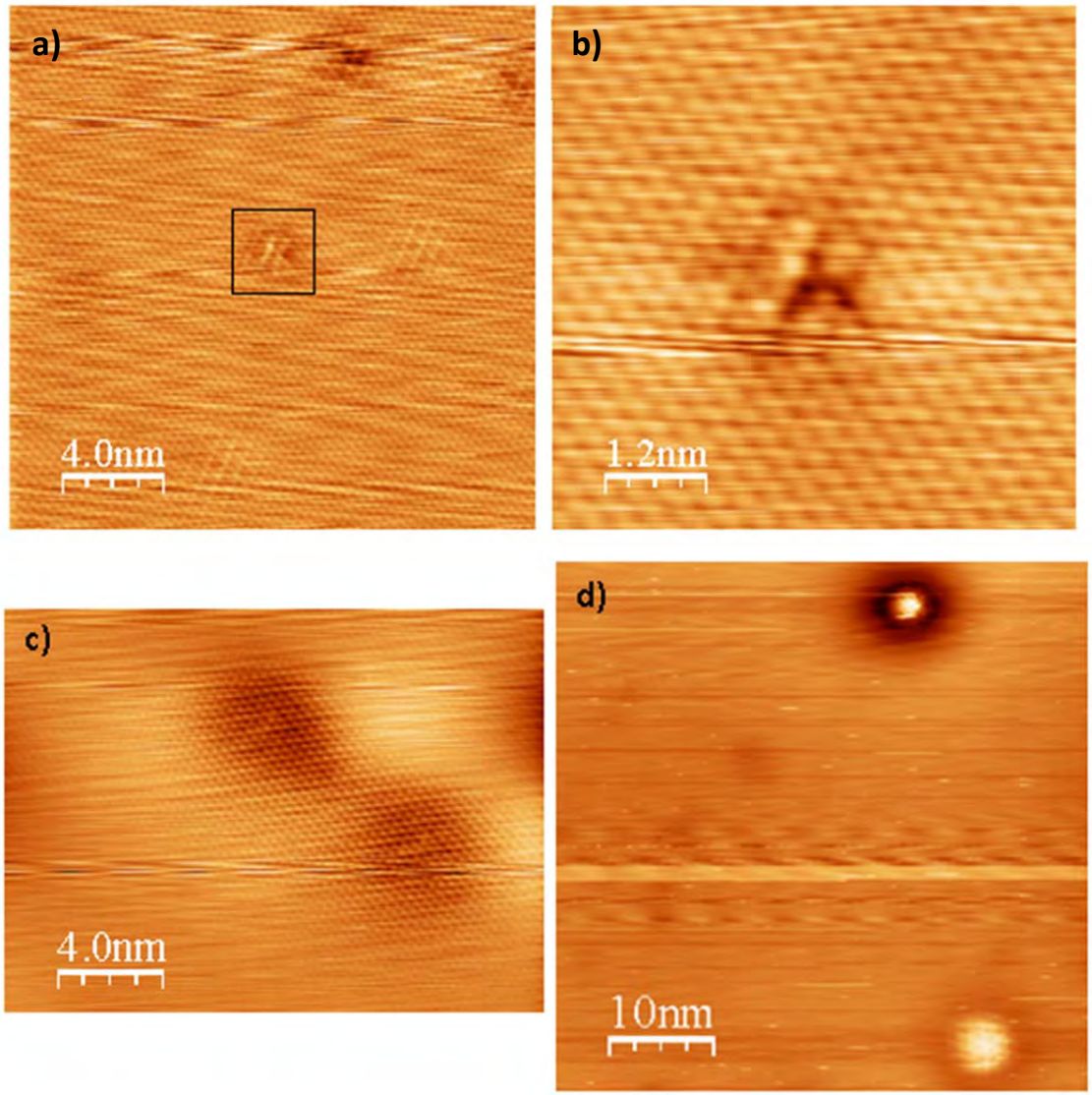

Figure 3.5 (a) 20 nm × 20 nm STM image of MoS_2 showing the ripple defects taken at a tip bias of 1.6 V. (b) 8 nm × 8 nm STM image taken of the defect marked by the square at a tip bias of 1.2 V. (c) 20 nm × 15 nm STM image of MoS_2 showing the ripple defects taken at a tip bias of 1.2 V. Note the alternating regions of undulations. (d) 50 nm × 50 nm STM image of MoS_2 showing the nanocluster defects taken at a tip bias of 1.5 V.

Figure 3.5d demonstrates two of the nanocluster-like defects. Bias-dependent imaging of the bottom defect in Figure 3.5d was carried out, and is given in Figure 3.6 When the defect was imaged at a positive tip bias, it was observes as a central protrusion surrounded by an annular depression. However, when the defect was imaged at a negative tip bias, it appears as a relatively flat structure consisting of atoms in the same period as normal MoS_2 thin film, with the ring structure absent. There was a marked difference in height of the defect centre with scanning bias, 47.8 pm at a negative tip bias of -0.4 V and 281 pm at a positive tip bias of 1 V

(Figure 3.7a). Furthermore, the bright protrusions under positive tip biases shows a hexagonal feature, which becomes progressively pronounced as the bias increased. The hexagonal feature was observed to be made up of 7 smaller round nanoclusters with a short-range periodicity of about 8 Å at a tip bias of +1.5 V. These variations would not be possible if the underlying cause was a purely topographical one; this change with varying tip bias is likely to be due to the variation in electronic density of states on the defect. Imaging of the top defect also displayed similar bias-dependent effect, with the same magnitude of difference of centre peak height observed. At a negative tip bias of -0.4 V, the height of the centre peak was 51.3 pm, and at a positive tip bias of 1.2 V, the height was 443 pm (Figure 3.7b).

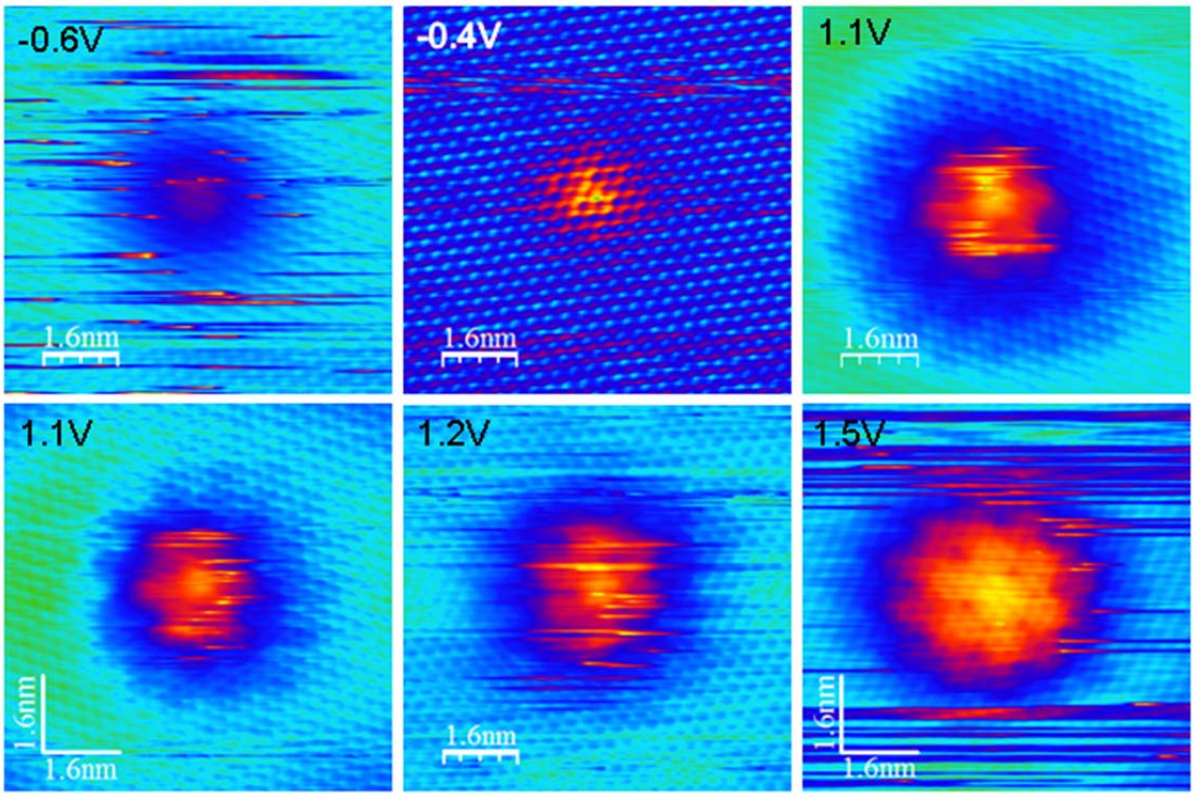

Figure 3.6 8 nm × 8 nm bias-dependent STM images of the bottom defect in Figure 3.5d with tip bias from -0.6 V (top left) to 1.5 V (bottom right).

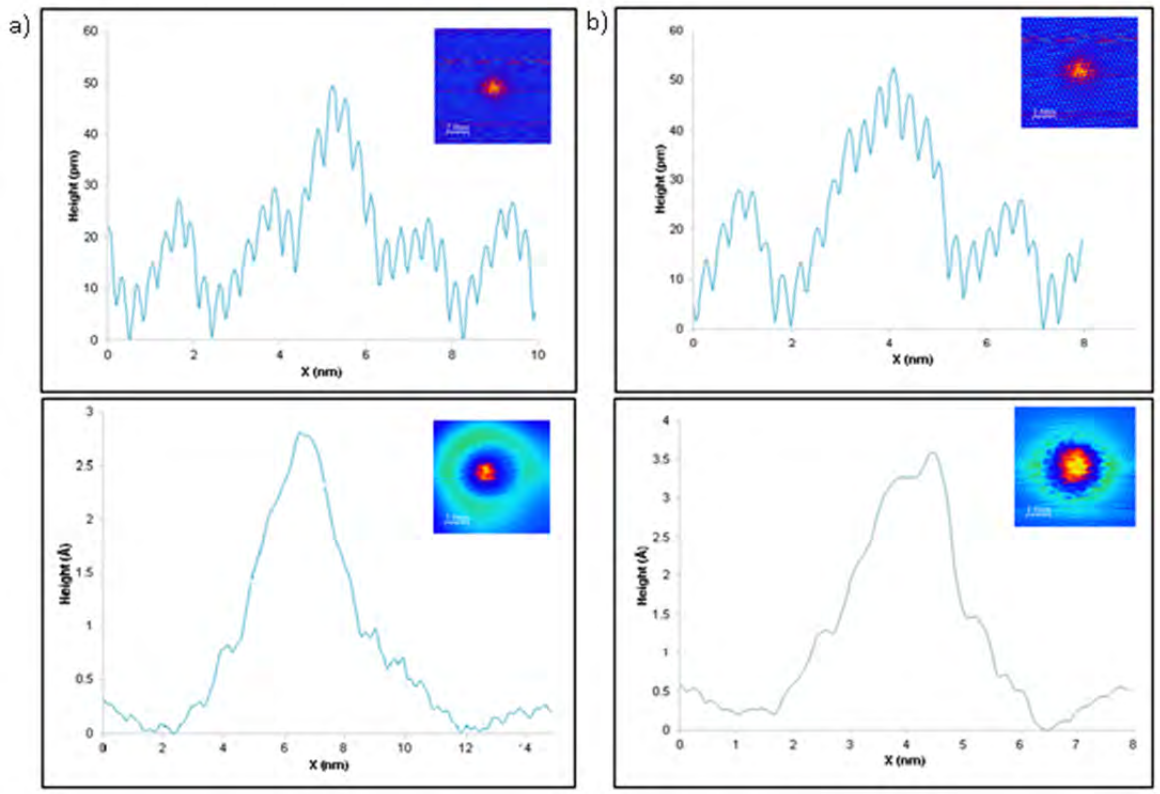

Figure 3.7 (a) Height profile of the bottom defect at a tip bias of -0.4 V (top) and 1 V (bottom). (b) Height profile of the bottom defect at a tip bias of -0.4 V (top) and 1.2 V (bottom). Insert are the corresponding STM images.

To probe the electronic properties of these defects, STS measurements were taken at different positions (Figure 3.8). A lock-in voltage modulation of 625 Hz and 40 mV was applied for the conductance measurement. In both instances of the nanocluster defects, the bandgap of 1.45 eV, corresponding to that of few-layered crystalline MoS_2, was preserved. It is noted that the bandgap is asymmetric about the Fermi level, where the conduction band minimum pinning at about 0.3 eV below $E_{f,}$ similar to the spectrum obtained from the mechanically exfoliated sample. However, as we probe closer to the defect centre, we observe the appearance of an additional energy state at about 0.3 eV above the valance band. Given that it is an *ex situ* sample, impurities of the p-type might be the cause of these defect. These p-type impurities form a carrier trap just above the valance band maxima which allows for the capture of electrons, creating a mid-gap state, and thus the observed additional energy state.

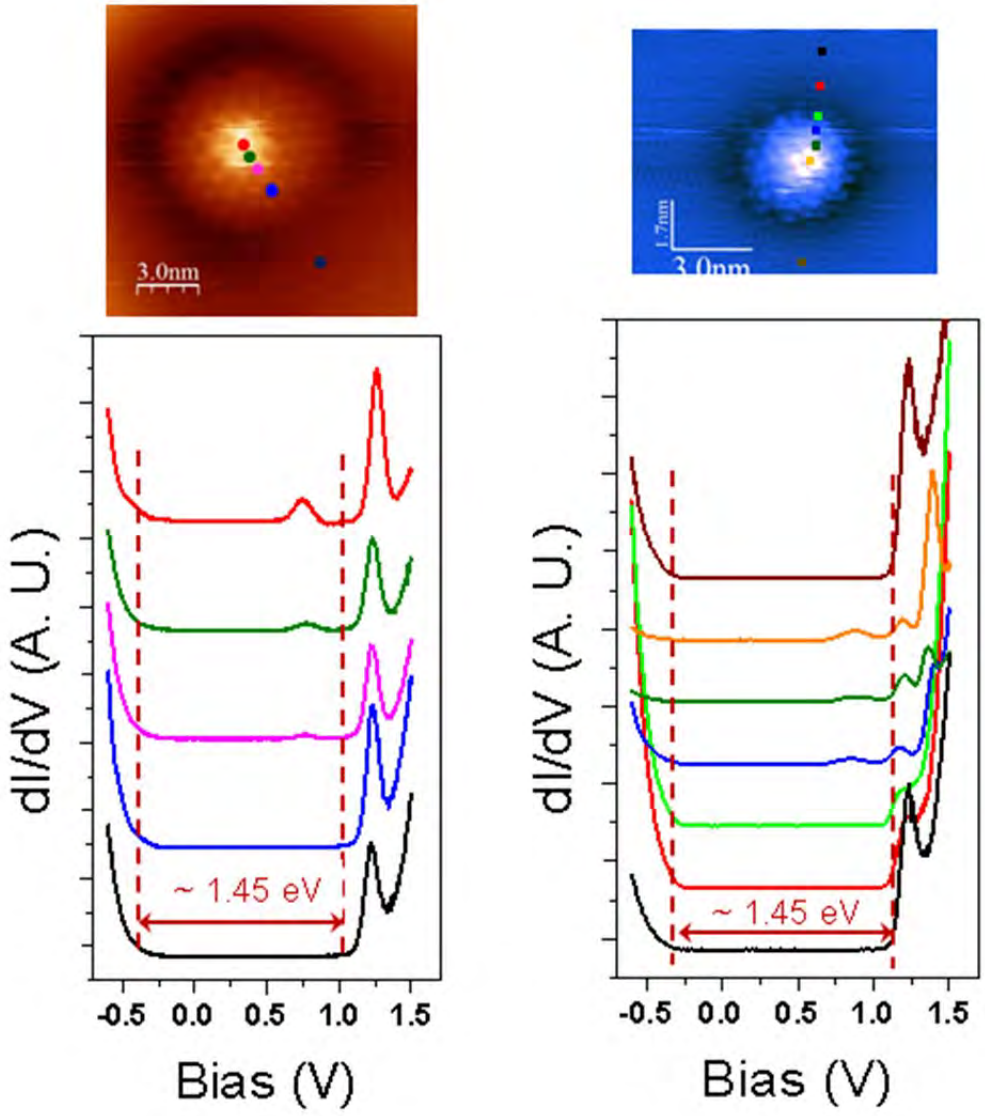

Figure 3.8 STS of the bottom (left) and top (right) defects. As we probe closer to the centre peak, we observe an additional peak within the bandgap, at about 0.3 eV above the valance band.

3.3 Chemical Vapour Deposition growth of MoS_2 (Direct/Transferred)

Another common method in fabricating MoS_2 thin films is via the bottom-up approach of chemical vapour deposition. This is accomplished by evaporating its precursors, such as molybdenum oxide and sulfur, whereby the vapours formed will react and form the desired material on a pre-positioned substrate. The advantages that CVD growth confers over the mechanically exfoliated method is scalable growth and systematic control of the film thickness and grain size[14, 16-17, 29-30].

We investigated the sample obtained from Prof Li-Lain-jong's group, Academia Sinica Taiwan[14], grown directly by the CVD method on HOPG. Large-scale STM image shows that the HOPG surface was not fully covered with MoS_2 flakes and the size of flakes average around hundreds of nanometers. Height profile analysis (not shown here) of the sample confirms the presence of monolayer films with thickness of about 7 Å, while analysis of the lattice constant confirms the films to be MoS_2. Large scale STM imaging reveals that the MoS_2 sample was decorated with numerous point defects (Figure 3.9a and 3.9b), with up to 1% of the surface area having the defects. To probe the electronic structure of the MoS_2 monolayer, STS with a lock-in modulation of 625 Hz and 40 mV was carried out on the sample. This produces a bandgap of about 2.40 eV for this direct CVD grown sample as shown in Figure 3.9c.

High resolution images of the MoS_2 thin film were taken, where bias-dependent imaging of the same area was carried out as shown in Figure 3.10. It was found that these defects manifests as holes at tip biases of -0.6 V and 1.5 V, while at a tip bias of 2.2 V, doughnut features with diameter of about 1.60±0.2 nm around the holes can be seen (Figure 3.10, top). In the dI/dV map in the bottom of Figure 3.10, interference patterns due to electron scattering off the defects is observable at -0.6 V. No distinguishable feature corresponding to the defects can be seen at 1.5 V, while the lower dI/dV contrast surrounding the defects is in contrast to the STM topographical map at 2.2 V. According to the electronic structure calculations using the density functional theory as calculated by Liu *et al.* [31], single sulfur vacancies defects are the most common vacancy defects on the surface due to having the lowest formation energy of 2.35 eV amongst the other point vacancy defects such as a single Mo vacancy with formation energy of 8.02 eV. As indicated by Zhou *et al.*[32], it is easy for a single Mo vacancy to lose also its three surrounding sulfurs to form a MoS_3 vacancy, which is not the

case we observed here. Thus, the vacancies observed in the sample are possible to be single sulfur vacancies.

A moiré pattern of period 1.24±0.02 nm was also observed in the STM images at tip biases of -0.6 V and 1.5 V in Figure 3.10a and 3.10b, corresponding to the theoretical calculated value of 1.15 Å with a low discrepancy of 7.8% (see Appendix A for detailed calculation). The moiré pattern was not visible in at Figure 3.10c as there was a larger tip-sample separation, and hence a poorer resolution at higher tip bias. The presence of similar moiré pattern with the same orientation and periodicity across various grains indicates that the MoS_2 monolayer grows at a fixed orientation to the HOPG substrate.

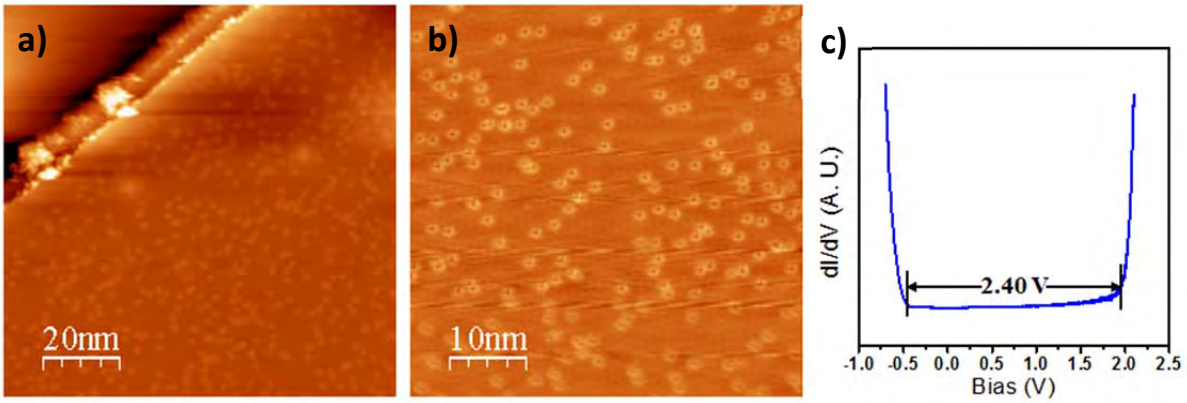

Figure 3.9 (a) 100 nm × 100 nm and (b) 50 nm × 50 nm STM image of the direct-grown MoS_2 monolayer showing numerous point defects present. Both images taken at a tip bias of 2.2 V. (c) Bandgap of the sample as obtained via STS.

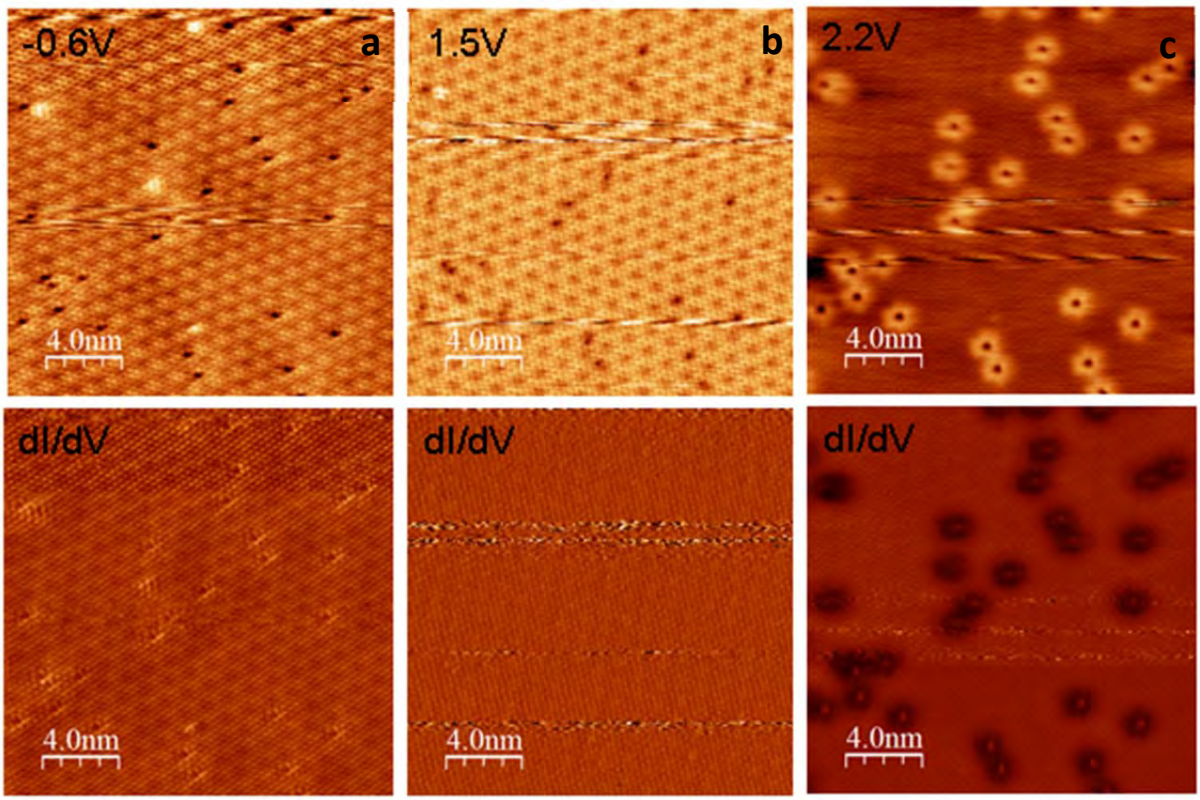

Figure 3.10 20 nm × 20 nm bias-dependent STM imaging of the defects with tip bias of (a) -0.6 V, (b) 1.5 V and (c) 2.2 V, with their corresponding dI/dV map at the bottom. Both STM images and dI/dV maps show that there is a region of low local density of state surrounding the defects at 2.2 V tip bias, which is absent at 1.5 V and at negative tip biases.

As an extension to the direct CVD growth method, the thin film can also be grown on another substrate, such as SiO_2/Si, first before being transferred onto an intermediate medium - usually Poly(methyl methacrylate) or PMMA - before finally transferred to the desired substrate. A transferred sample from Prof Eda Goki's group, National University of Singapore, is demonstrated in Figure 3.11 and Figure 3.12. The transferred MoS_2 was first grown on a Si substrate with 300 nm SiO_2 coating. Thereafter, PMMA was coated onto the sample which was later immersed in KOH where the MoS_2 attached to the PMMA delaminates from the silicon substrates and floats. The MoS_2 sample, which is still attached to the PMMA, was then transferred onto HOPG to be cleaned with acetone to remove the PMMA. From the optical image of the sample as shown in Figure 3.11, we observe large monolayer MoS_2 flakes of about 50 μm on the HOPG substrate.

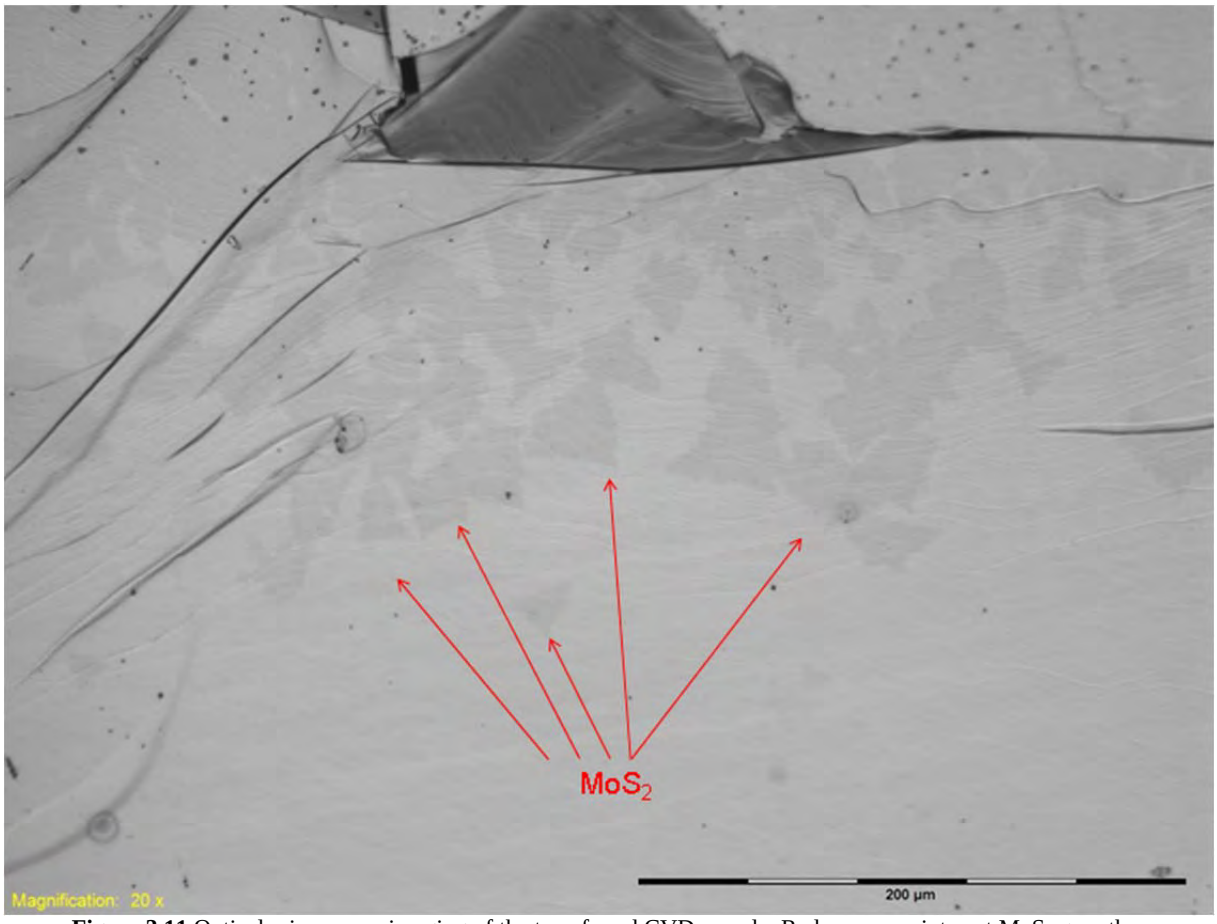

Figure 3.11 Optical microscopy imaging of the transferred CVD sample. Red arrows points out MoS_2 growths.

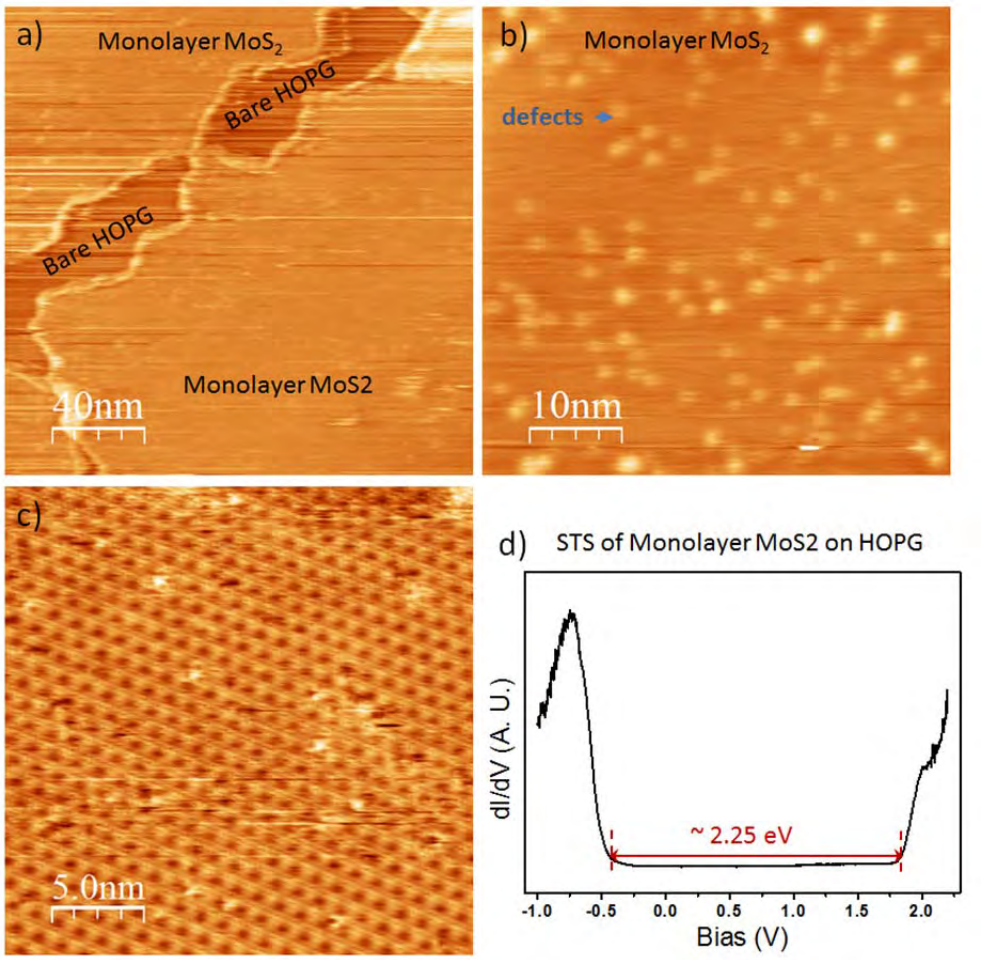

Figure 3.12 (a) 200 nm × 200 nm, (b) 50 nm × 50 nm, and (c) 20 nm × 20 nm STM image of the transferred MoS_2 monolayer showing numerous point defects present. Images taken at a tip bias of (a) 1.9 V, (b) 2 V and (c) -1.2 V. (d) Bandgap of the sample as obtained via STS.

Detailed investigations of the transferred sample found that it is similar to the one grown directly, as shown in the STM images in Figure 3.12. Defects seen in Figure 3.12b were observed with similar features as those seen earlier in Figure 3.9 and 3.10. The moiré pattern in this sample as seen in Figure 3.12c has the same period of about 1.2 nm as the direct-grown sample as observed in Figure 3.10. However, the bandgap of this sample, 2.25 eV, (Figure 3.12d), found using the same STS parameters, is slightly smaller than that of 2.4 eV (Figure 3.9c). This difference is possibly caused by contamination in the transfer process. Both bandgaps measured are much higher than the theoretical value of 1.8 eV with percentage discrepancies of 33.3% and 25% for the direct-grown and transferred MoS_2

respectively. These large discrepancies could be due to the formation of excitons[33]. Another possible cause could be a suboptimal tip condition, such as the adsorption of a foreign atom across the tunneling pathway, thus affecting the density of states.

Both CVD methods used to fabricate MoS_2 films were found to be of similar quality in terms of the concentration of defects, which is less than the sample fabricated using the mechanical exfoliation method. However, the direct CVD method yields the smallest grains of the three methods, of hundreds of nanometers in size. The transferred CVD method is clearly the superior method, with a larger area of more consistent single-layered growth and fewer defects. Critical observations of all three *ex situ* methods summarized as below:

	Mechanically Exfoliated	**Direct CVD**	**CVD Transferred**
Size	~20 μm	~100 nm	~50 μm
Layers	Few	Single	
Growth	Ordered	Ordered	
Defects	10% of surface, 2 nm -10 nm ripples and nanocluster defects	1% of surface, single sulfur point vacancies	

Table 3.1 A comparison of the quality of the resulting MoS_2 using the three methods examined thus far.

3.4 *In situ* UHV CVD growth of MoS_2

While CVD is an established method in the fabrication of MoS_2 thin film, the growth process is still not well understood and thus remains challenging to obtain controlled crystalline growth[34]. In order to further understand the growth mechanics of MoS_2, reduce contaminations and improve on the quality of growth, we attempt to grow MoS_2 thin film *in situ* in our UHV chamber.

A total of five growth attempts of MoS_2 fabrication on Ag(111) substrate were carried out by first depositing MoO_3 on a clean substrate to form an oxide film, followed by depositing

sulfur. This oxide film is made up of $(MoO_3)_x$, where $x = 3, 4, 5$, have been previously detected in mass spectrometric studies MoO_3 sublimation by Demaria *et al.*[35]. The Ag(111) substrate was cleaned via several cycles of Ar^+ ion sputtering at 500 V to 1000 V and annealing. STM imaging of the substrate was used to confirm the cleanliness. Once the substrate was cleaned, MoO_3 was deposited at 480 ^oC for durations of 1 min to 10 min for various samples to vary the thickness of $(MoO_3)_x$ grown. Subsequently, sulfur was deposited onto the $(MoO_3)_x$ thin film at 50 ^oC for durations varying from 20 s to 1 min. The samples were then checked by the STM after each step. After each deposition cycle of MoO_3 or S, the sample was allowed to be annealed to eliminate stress and achieve an equilibrium state. All steps of the experiments were carried out in the preparation chamber under UHV condition to minimize contamination.

In all the growth attempts, the intermediary, $(MoO_3)_x$, was successfully grown on the Ag(111) substrate. We observed three types of structure being formed: an ordered hexagonal nanoarray, 3-lobed triangular and 4-lobed square nanoparticles, depending on the $(MoO_3)_x$ coverage, as well as the absorption sites.

In Figure 3.13, a closely packed hexagonal nanoarray with a periodicity of 1.21±0.02 nm on the Ag(111) terrace is formed. About 2% defects are randomly distributed over the surface, including vacancies with a dark contrast and absorbates with bright protrusions. The absorbates are observed to be of two sizes, either the same, or twice the size of the nanodots. A spontaneous tip change during one of the scanning reveals a 6- or 5-lobed fine structure of each nanodot in this close-packed nanoarray (Figure 3.14).

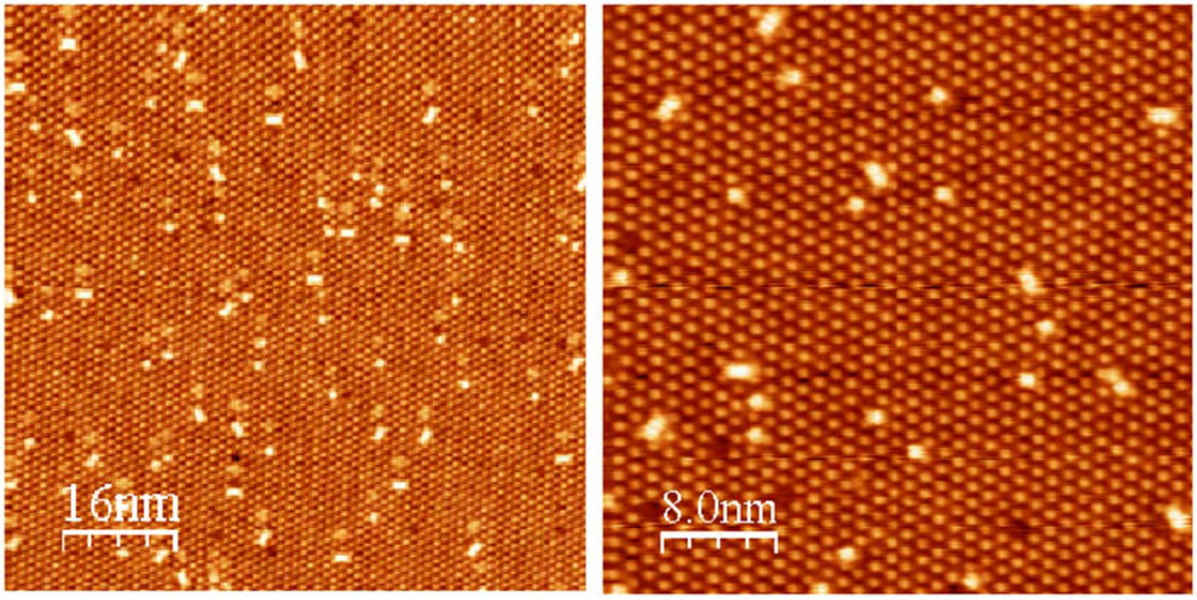

Figure 3.13 80 nm × 80 nm (left) and 40 nm × 40 nm STM images of the regular hexagonal lattice with vacancy and adsorption of additional absorbates. Images taken at a tip bias of -2.5 V (left) and 2.5 V (right).

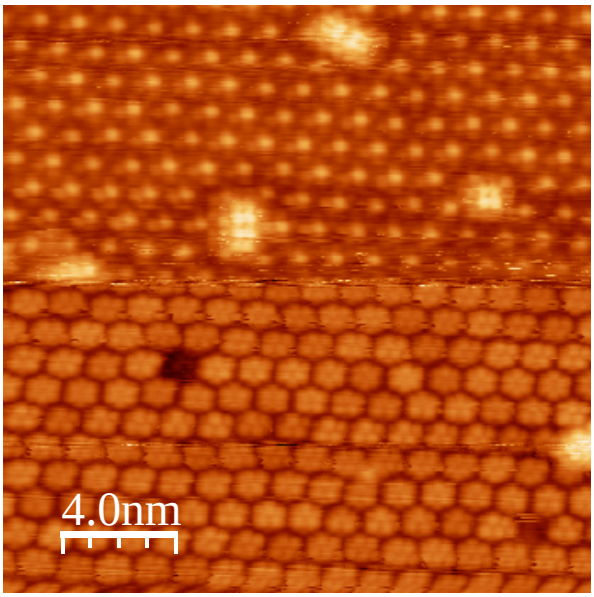

Figure 3.14 20 nm × 20 nm STM image taken at tip bias of 2 V. A spontaneous tip change mid-scan reveals an underlying 5- or 6-lobed fine structure.

The 3-lobed triangular nanoparticles were often observed at Ag(111) terraces with low coverage. In Figure 3.15, these nanoparticles show a three-fold symmetry and are 1.21±0.2 nm in size. They were observed to grow in two main orientations, with one of the lobe pointing either towards or away from the <1 -1 0> direction of the silver substrate. These triangular nanoparticles are not closely packed and were observed to be isolated from each other.

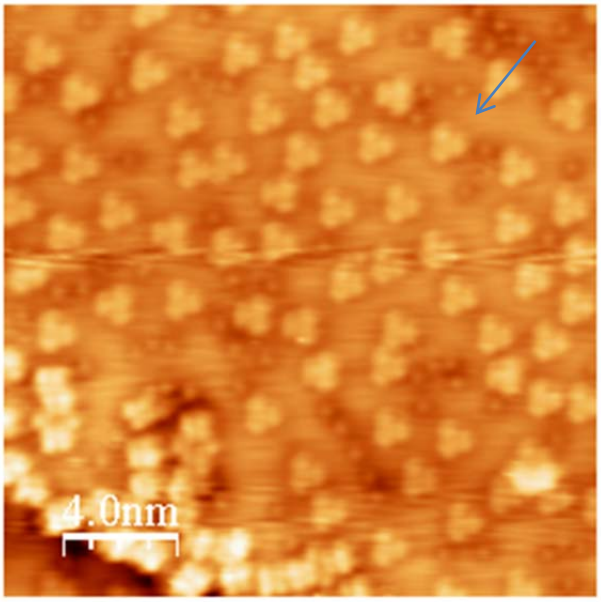

Figure 3.15 20 nm × 20 nm STM image of 3-lobed triangular nanoparticles on Ag(111) taken at a tip bias of -0.5V. The nanoparticles are not closely packed, and they grow with one lobe either pointing towards or away from the <1 -1 0> direction of the underlying substrate (indicated by the blue arrow).

The third type of structure, the 4-lobed square nanoparticles of size about 1.20±0.02 nm, was mainly seen on the Ag(111) edges, indicating higher formation energy is required. As previously observed by Monika *et al.*[36], the formation of these nanoparticles tends to be parallel to the edge of the steps, indicating a more energetically favorable orientation (Figure 3.16).

At certain conditions, with high coverage, these 4-lobed nanoparticles are capable of forming a closed packed nanostructure with the 3-lobe nanoparticles. A repeating unit consisting of four nanoparticles is then formed, each consisting of a 3-lobed nanoparticle at the centre and a 4-lobed nanoparticle at the end of each lobe, with a periodicity of 2.88±0.02 nm as seen in Figure 3.17, ten times of silver's 2.89 Å lattice constant. The direction of growth of this repeating unit does not follow that of the underlying substrate, instead, growing with one of the axis at 34±3^{o} from the Ag <1 -1 0> direction.

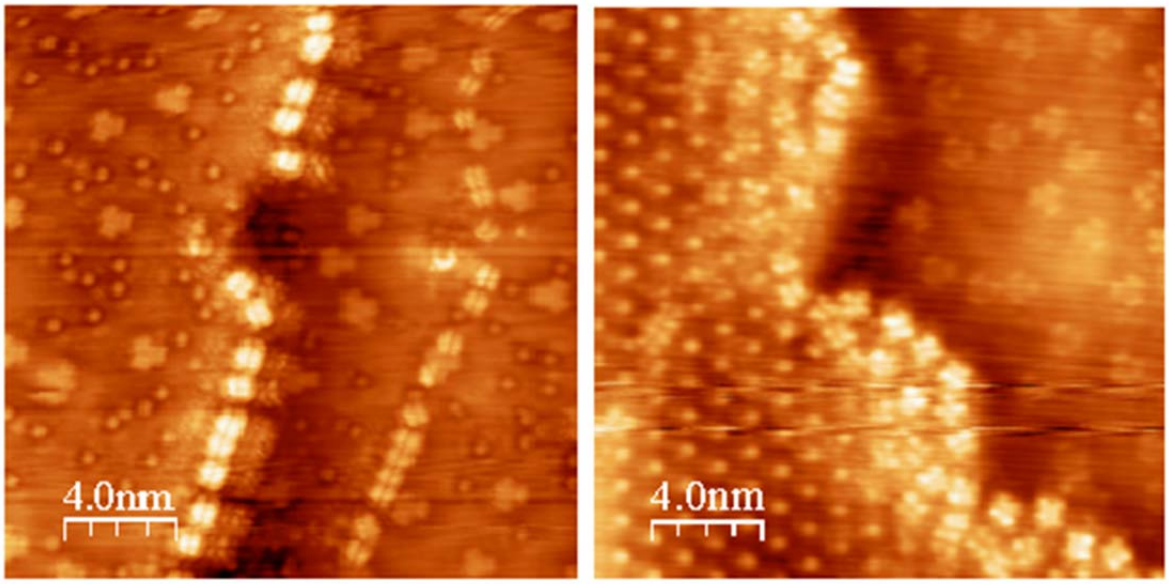

Figure 3.16 20 nm × 20 nm STM images of the 4-lobed nanoparticles growing at the edge of a terrace (left) and a hole (right). Images were taken at a tip bias of 1.6 V (left) and -0.8 V (right).

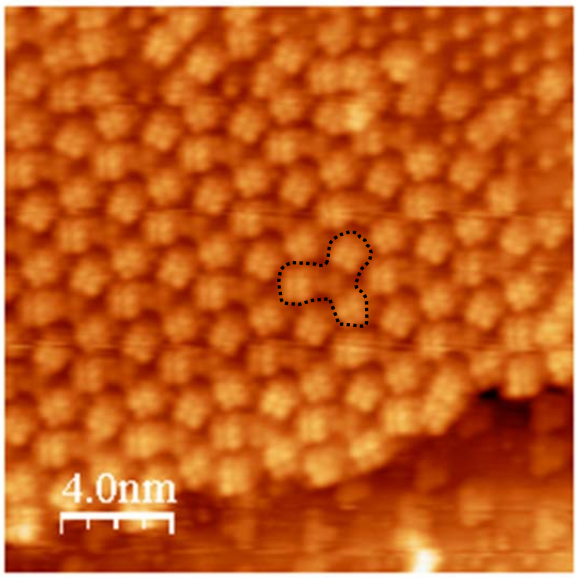

Figure 3.17 20 nm × 20 nm STM image taken at tip bias of 0.5 V. A repeating unit (dotted outline), consisting of a 3-lobed nanoparticle at the centre with a 4-lobed nanoparticle at each of the lobes, with a period of about 2.88 nm can be observed. They were grown with one of the axis 34^{o} from the Ag <1 -1 0> direction.

Subsequent depositions of sulfur onto the $(MoO_3)_x$ oxide film usually remove most oxides from the substrate, giving a clean surface with no MoS_2 observed. This indicates that the sulfur could have reacted with the $(MoO_3)_x$ oxide film, but the product did not adhere to the substrate, and might have been drawn out by the vacuum pump. More attempts with varied conditions will be carried out in the near future.

References

1 Mak, K. F.; Lee, C.; Hone, J.; Shan, J.; and Heinz, T. F; *Phys. Rev. Lett.* **105**, 136805 (2010).

2 Splendiani; A.; Sun, L.; Zhang, Y.; Li, T.; Kim, J.; Chim, C.; Galli, G.; and Wang, F.; *Nano Lett.* **10**, 1271–1275 (2010).

3 Claus, F. L.; *Solid Lubricants and Self-Lubricating Solids (Academic Press, 1972).*

4 Kam, K. K.; and Parkinson, B. A; *J. Phys. Chem.* **86**, 463–467 (1982).

5 Lebegue, S.; and Eriksson, O.; *Phys. Rev. B* **79**, 115409 (2009).

6 Mak, K. F.; Lee, C.; Hone, J.; Shan, J.; and Heinz, T. F.; *Phys. Rev. Lett.* **105**, 136805 (2010).

7 Kuc, A.; Zibouche, N.; and Heine, T.; *Phys. Rev. B* **83**, 245213 (2011).

8 Young, P. A.; *J. Phys. D: Appl. Phys.***1** 936 (1968).

9 Frindt, R. F.; *J. Appl. Phys.* **37**, 1928–1929 (1966).

10 Novoselov, K. S.; Jiang, D.; Schedin, F.; Booth, T. J.; Khotkevich, V. V.; Morozov, S. V.; and Geim, A. K.; *Proc. Natl. Acad. Sci. USA* **102**, 10451-10453 (2005).

11 Joensen, P.; Frindt, R. F.; and Morrison, S. R. *Mater. Res. Bull.* **21**, 457–461 (1986).

12 Schumacher, A.; Scandella, L.; Kruse, N.; and Prins, R.; *Surf. Sci. Lett.* **289**, L595–L598 (1993).

13 Coleman, J. N.; Lotya, M.; O'Neill, A.; Bergin, S. D.; King, P. J.; Khan, U.; Young, K.; Gaucher, A.; De, S.; Smith, R. J.; et al.; *Science* **331**, 568–571 (2011).

14 Liu, K. K.; Zhang, W. J.; Lee, Y. H.; Lin, Y. C.; Chang, M. T.; Su, C.; Chang, C. S.; Li, H.; Shi, Y. M.; Zhang, H.; Lai, C. S.; and Li, L. J.; *Nano Lett.* **12**, 1538 (2012).

15 Lin, Y. C.; Zhang, W. J.; Huang, J. K.; Liu, K. K.; Lee, Y. H.; Liang, C. T.; Chu, C. W.; and Li, L. J.; *Nanoscale* **4**, 6637 (2012).

16 Lee, Y. H.; Zhang, X. Q.; Zhang, W. J.; Chang, M. T.; Lin, C. T.; Chang, K. D.; Yu, Y. C.; Wang, J. T. W.; Chang, C. S.; Li, L. J.; and Lin, T.W.; *Adv. Mater.* **24**, 2320-2325 (2012).

17 Zhan, Y. J.; Liu, Z.; Najmaei, S.; Ajayan, P. M.; and Lou, J.; *Small* **8**, 966 (2012).

18 Xiao, D.; Liu, G.-B.; Feng, W.; Xu, X.; and Yao, W; *Phys. Rev. Lett.* **108**, 196802 (2012).

19 Cao, T.; Wang, G.; Han, W.; Ye, H.; Zhu, C.; Shi, J.; Niu, Q.; Tan, P.; Wang, E.; Liu, B.; and Feng, J.; *Nature Commun.* **3**, 887 (2012).

20 Zeng, H.; Dai, J.; Yao, W.; Xiao, D.; and Cui, X.; *Nature Nanotech.* **7**, 490–493 (2012).

21 Mak, K. F.; He, K.; Shan, J.; and Heinz, T. F.; *Nature Nanotech.* **7**, 494–498 (2012).

22 Helveg, S.; Lauritsen, J. V.; Lægsgaard, E.; Stensgaard, I.; Nørskov, J. K.; Clausen, B. S.; Topsøe, H.; and Besenbacher, F.; *Phys. Rev. Lett.* **84**, 951-954 (2000).

23 Lauritsen, J. V.; Kibsgaard, J.; Helveg, S.; Topsøe, H.; Clausen, B. S.; Lægsgaard, E.; and Besenbacher, F.; *Nat Nanotechnol* **2**, 53-58 (2007).

24 Radisavljevic, B.; Radenovic, A.; Brivio, J.; Giacometti, V.; and Kis, A; *Nat. Nanotechnology* **6**, 147−150 (2011).

25 Radisavljevic, B.; Whitwick, M. B.; and Kis, A.; *ACS Nano***5**, 9934−9938 (2011).

26 Brivio, J; Alexander, D. T. L. and Kis, A.; *Nano Lett.* **11**, 5148−5153 (2011).

27 Obeng, Y.; Gendt, S. D.; Srinivasan, P.; Misra, D.; Iwai, H.; Karim, Z.; Hess, D. W.; and Grebel H.; *ECS Transactions* **19(5)**, 79 (2009).

28 Meyer, J. C.; Geim, A. K.; Katnelson, M. I.; Novoselov, K. S.; Booth, T. J.; and Roth, S.; Nature **446**, 60-63 (2007).

29 Helveg, S.; Lauritsen, J. V.; Lægsgaard, E.; Stensgaard, I.; Nørskov, J. K.; Clausen, B. S.; Topsøe, H.; and Besenbacher, F.; *Phys. Rev. Lett.* **84**, 951-954 (2000).

30 Shi, Y.; Zhou, W.; Lu, A-Y.; Fang, W. Lee, Y-H., Hsu, A. L.; Kim, K. K.; Yang, H. Y.; Li, L-J.; Idrobo, J-C.; and Kong, J.; *Nano Lett.***12(6)**, 2784–2791 (2012).

31 Liu, D.; Guo, Y.; and Robertson, J.; *Appl. Phys. Lett.* **103**, 183113 (2013).

32 Zhou, W.; Zou, X.; Najmaei, S.; Liu, Z.; Shi, Y.; Kong, J.; Lou, J.; Ajayan, P. M.; Yakobson, B. I.; and Idrobo, J-C.; *Nano Lett.* **13 (6)**, 2615–2622 (2013).

33 Ye. Y.; Ye, Z.; Gharghi, M.; Zhu, H.; Zhao, M.; Yin X.; and Zhang, X.; *arXiv*:1305.4235

34 Wang, X.; Feng, H.; Wu, Y.; and Jiao, L.; *J. Am. Chem. Soc.* **135**, 5304-5307 (2013).

35 DeMaria, G.; Burns, R. P.; Dowart, J.; and Inghram, M. G.; J. Chem. Phys. **32**, 1373 (1960).

36 Biener, M. M.; Biener, J.; Schalek, R.; and Friend, C. M.; *J. Chem. Phys.* **121**, 12010 (2004).

Chapter 4: Conclusion and Outlook

4.1 Thesis Summary

In this thesis, we investigated the surface structural and electronic properties of single- to few-layered MoS_2 on HOPG substrates obtained via three different preparation methods. Scanning tunneling microscopy and spectroscopy measurements are used to visualize the physical and electronic structures at the surface. *In situ* growth of MoS_2 on Ag(111) surfaces were also attempted.

In the first method, the few-layered MoS_2 was mechanically exfoliated and deposited onto a HOPG substrate. This yielded regions of about 20 μm of few-layered MoS_2. This MoS_2 sample was found to be with a relatively defect-rich, present on about 10% of the surface area, with sizes of the defects ranging from 2 nm to 10 nm. Extensive defects manifested as ripples and nanoclusters, modifying the topographical images obtained by STM. Possible causes of these defects were thought to be the presence of vacancies, impurities, or excess stress.

In the second method, MoS_2 was grown directly onto HOPG using the CVD method. This sample consisted of MoS_2 monolayers of about hundreds of nanometers in size. On about 1% of the sample surface, there were observable defects. These defects appear as different features under different scanning biases, and are attributed to single sulfur vacancies. The bandgap of the monolayers was also determined using STS to be about 2.4 eV.

In the third method, MoS_2 was grown using CVD which is then chemically transferred onto HOPG. This sample contains ~50 μm MoS_2 monolayers and its bandgap was determined at about 2.25 eV.

In both CVD grown samples, direct-grown and transferred, monolayer MoS_2 were observed to have defects of the same nature, present on about 1% of the surface area. In addition, moiré

patterns corresponding to the lattice mismatch of MoS_2 and the underlying HOPG substrate of about 1.2 nm were also observed.

In light of the defects present in the above mentioned MoS_2 samples created through mechanical exfoliation and CVD, a fourth method, *in situ* ultrahigh vacuum growth, was attempted in hopes of improving the quality of production, with more consistent and larger area of monolayer growth with fewer defects. Using this method, we were able to consistently obtain $(MoO_3)_x$ intermediates on Ag(111) substrates, with recurring 4-lobed and 3-lobed nanoparticles and regular hexagonal nanoarrays. However, we were unable to obtain MoS_2 after evaporating sulfur onto the intermediary oxide film so far. More intensive efforts will be devoted to this *in situ* growth.

4.2 Future Work

Although this thesis has discussed the effects of various fabrication methods on the electronic and crystalline structural of MoS_2 thin films, an incomplete control of these processes and an incomplete understanding of the different growth parameters have resulted in a less than ideal product. To successfully achieve consistent, high quality growth of MoS_2 thin films, and to understand the nature of the defects present using these methods, further studies need to be carried out with varying growth parameters.

In order to better understand the underlying principles of the formation of the defects, different modeling methods and types of analysis can be used. Such methods include theoretical simulations of the surface structure, and its interactions with the underlying substrates using a computational modeling method such as the density functional theory or the Hartree-Fock theory.

Also, complementary experimental methods should also be used to study the thin films. Low-energy electron diffraction (LEED) could be used to verify the lattice structure and spacing. Another complementary experimental method would be angle-resolved photoemission spectroscopy (ARPES) to probe and verify the Fermi surface and the band structure of the thin film.

Instead of using the Ag(111) substrate during the *in situ* CVD fabrication of MoS_2, which the product does not adhere well to, a different substrate could be used to enhance the adhesion so as to ensure the product will not be lost.

MoS_2 is not the only TMD with potential applications in the electronic industry. Future work should also look into other TMDs, such as $MoSe_2$, for potential fabrication opportunities. As the precursors of $MoSe_2$ have a similar volatility, variations in the current CVD method used such as simultaneous deposition can also be studied.

Appendix A

The theoretical period of the moiré pattern resulting from overlaying an MoS_2 monolayer on a HOPG substrate was calculated using the following equation:

$$D = \frac{d_1 d_2}{\sqrt{d_1^2 + d_2^2 - 2d_1 d_2 cos\theta}}$$

The following parameters were used:

Period of HOPG: $d_1 = 2.46$ Å

Period of MoS_2: $d_2 = 3.13$ Å

Angle between the two lattices: $\theta = 0^0$

The moiré period, D, was then found to be 11.5 Å.